# **Advanced Non-Adiabatic Flamelet-based Combustion and Heat Transfer Model for Rocket Engine Thrust Chambers**

Marvin Pommerening\*<sup>†</sup>, Daniel Eiringhaus\* and Chiara Manfletti<sup>†</sup>

\*ArianeGroup GmbH, Robert-Koch-Str. 1, 82024 Taufkirchen, Germany

<sup>†</sup>Technical University of Munich, Chair of Space Mobility and Propulsion, Lise-Meitner-Str. 9-11, 85521 Ottobrunn,

Germany

marvin.pommerening@ariane.group · daniel.eiringhaus@ariane.group · chiara.manfletti@tum.de

# **Abstract**

In the present study, the performance of a propellant-independent multi-dimensional flamelet model for the simulation of highly non-isobaric and cooled reacting rocket thrust chamber flows is analyzed with respect to combustion and wall heat transfer characteristics. For this purpose, the modeling framework is applied to a selected experimentally investigated subscale single-flame configuration incorporating methane combustion and nozzle expansion, which provides validation data in terms of wall pressure and heat flux profiles. These are satisfactorily reproduced by the flamelet model presented. The entire relevant enthalpy space is adequately covered by the combination of multiple different non-adiabatic extension methods.

## Nomenclature

```
specific isobaric heat capacity [J kg<sup>-1</sup> K<sup>-1</sup>]
                                                                              density [kg m<sup>-3</sup>]
c_p
Da
            Damköhler number [–]
                                                                              time scale [s]
                                                                              generic quantity [-]
h
        = specific absolute enthalpy [J kg<sup>-1</sup>]
                                                                   φ
J
            momentum ratio [-]
                                                                              scalar dissipation rate [s<sup>-1</sup>]
                                                                   X
                                                                              net production rate [kg m^{-3} s<sup>-1</sup>]
            turbulent kinetic energy [m<sup>2</sup> s<sup>-2</sup>]
k
                                                                   \dot{\omega}
                                                                              volumetric heat release rate [W m<sup>-3</sup>]
L
            total chamber length [m]
                                                                   \dot{\omega}_T
Le
        = Lewis number [-]
                                                                   Subscripts
l
        = length [m]
                                                                                      quantity representative for chemistry
                                                                   chem
        = molecular weight [kg kmol^{-1}]
M
                                                                   con
                                                                                 =
                                                                                     contraction
            mass flow rate [kg s<sup>-1</sup>]
m
                                                                                 = cylindrical
                                                                   cyl
            oxidizer-to-fuel ratio [-]
O/F
                                                                                     expansion
                                                                   exp
P
            probability density function [-]
                                                                                     quantity at exit
                                                                   exit
            static pressure [Pa]
p
                                                                   flow
                                                                                     quantity representative for flow
Pr
        = Prandtl number [-]
                                                                   fu
                                                                                 =
                                                                                     fuel
        = heat flux [W m^{-2}]
ġ
R
           total chamber radius [m]
                                                                   i, j, k
                                                                                      spatial direction indices
            universal gas constant [J kmol<sup>-1</sup> K<sup>-1</sup>]
R
                                                                   inert
                                                                                      quantity in inert mixture
Sc
            Schmidt number [–]
                                                                   1b
                                                                                     last burning
T
            static temperature [K]
                                                                   min, max
                                                                                      minimum, maximum
        =
            time [s]
                                                                                      normalized
                                                                   norm
            velocity [m s<sup>-1</sup>]
и
                                                                                      outer
                                                                   0
            mixture fraction [-]
Z
                                                                                      oxidizer
                                                                   ox
Z''^2
        = mixture fraction variance [-]
                                                                   st
                                                                                      stoichiometric
        = spatial coordinates [m]
x, r
                                                                                      turbulent
Y
        = mass fraction [-]
                                                                                      quantity at throat
                                                                   throat
            turbulent dissipation rate [m<sup>2</sup> s<sup>-3</sup>]
                                                                                     quantity at wall
                                                                    wall
                                                                                 =
            area ratio [-]
ε
                                                                                     species index
            actual to nominal injection temperature ratio [-]
\zeta_{T_{\rm inj}}
                                                                    Superscripts
        = degree of frozen cool-down [-]
\theta_{\rm cool}
                                                                        = Reynolds average
            thermal conductivity [W m<sup>-1</sup> K<sup>-1</sup>]
λ
                                                                            Favre average
            dynamic viscosity [Pa s]
μ
                                                                            wall units
```

# 1. Introduction

Numerical simulations have become an integral part of today's development process of modern rocket engines. They enable the prediction of global performance characteristics and, moreover, profound physical understanding of the underlying thermochemical and fluid dynamic processes. On this basis, the design optimization process of the overall technical system and its sub-components as well as their reliability is continuously improved, while development costs and time are reduced in the long term<sup>11</sup>. The requirements for simulative tools are diverse and challenging. A wide variety of multi-physical phenomena and complex thermochemical processes, as well as their interplay, must be adequately reproduced in order to make useful statements and derive solid design guidelines. As an essential part of the propulsion system, the thrust chamber is of particular concern as it is usually subjected to severe thermal and mechanical loads. In order to prevent system failure and ensure safe operation, sophisticated cooling methods are crucial, the design of which demands precise predictions of the interaction between the flame and cooled walls as well as the resulting local heat flux distribution. Furthermore, the expansion process in throat and nozzle extension leads to an immense pressure gradient which ultimately makes an isobaric and adiabatic modeling approach inadequate. However, the reactive flow is also characterized by high Reynolds numbers and thus high turbulence, which interacts dynamically with the chemistry and decisively influences the flame characteristics, making its modeling even more difficult. All these phenomena must be taken into account in order to make reliable predictions, while keeping the computational effort at a minimum to allow the application in the industrial context.

Although the available computational power is steadily increasing, at least for chemically more complex propellants such as hydrocarbon or storable fuels with large reaction mechanisms and associated slow time scales of the chemical kinetics, tabulated chemistry is still a highly attractive approach in Computational Fluid Dynamics (CFD) applications. The widely used flamelet-based combustion model according to Peters<sup>18</sup> belongs to this category and constitutes the baseline for the present study. The decoupling of chemical and fluid dynamic computations allows the consideration of detailed reaction mechanisms and non-equilibrium chemistry at comparatively low numerical costs. This is achieved by generating thermochemical libraries in advance and coupling them to the flow solver via a reduced set of representative look-up variables. However, the classical flamelet modeling approach is not suitable for describing the flame-wall interactions as well as the wide range of described thermophysical states occurring in actively cooled rocket engine thrust chambers. Therefore, this paper analyzes and applies an advanced, higher-fidelity flamelet modeling framework allowing for non-adiabatic wall treatment while accounting for large pressure variations. In line with the ongoing development of the reusable motor Prometheus<sup>8</sup> at ArianeGroup dedicated to the next generation of European rocket launchers, the application will focus exclusively on a methane-fueled configuration, even if it is explicitly not limited to a specific propellant. As a fuel, methane offers a favorable combination of performance characteristics based on its chemical valency, manageability as well as decisive cost reduction potentials due to its availability and thermophysical properties and is therefore particularly suitable for future mission profiles<sup>5,10</sup>.

# 2. Experimental configuration

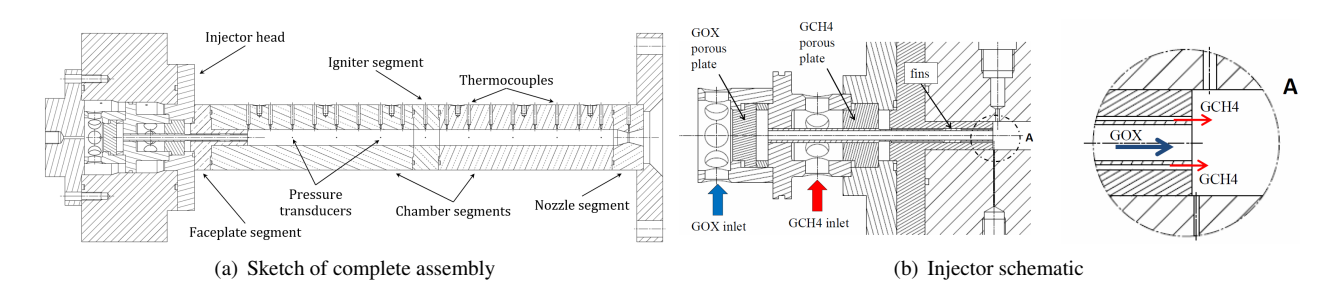


Figure 1: Experimental configuration of the TUM single-element combustor adapted from Silvestri et al.<sup>26</sup>

The object of investigation of the present study is the capacitively cooled single-element rocket engine subscale combustor with circular cross-section, which is operated with gaseous methane and oxygen and has been extensively studied experimentally at the Mobile Rocket Test Bench (*Mobiler Raketenprüfstand*) (MoRaP) at the Technical University of Munich (TUM). Figure 1 shows the modular structure of the combustion chamber consisting of injector head, faceplate, igniter, nozzle and multiple chamber segments as well as a detailed schematic of the injector. In the co-axial injector element configuration, the oxidizer is introduced into the combustion chamber through a central duct while the fuel is fed through the surrounding annular gap, where the mixing process of the propellants is triggered by the

destabilizing shear forces at the contact zone. The oxidizer post tip of the element variation considered has no tapering and no recess. Instead, it is flush-mounted with the faceplate. Homogenization of the inflow profiles in the injection plane is achieved by two integrated porous plates. In the convergent-divergent nozzle further downstream, the hot gas is finally expanded to ambient pressure, which ensures representative Mach numbers in the chamber. Table 1 gives an overview of some geometric key figures.

<b>D</b>	C1 1	X7.1 .	TT '4
Parameter	Symbol	Value	Unit
Oxidizer injector radius	$r_{ m O_2}$	2	mm
Inner fuel injector radius	$r_{\mathrm{CH_{4,i}}}$	2.5	mm
Outer fuel injector radius	$r_{\mathrm{CH_{4,0}}}$	3	mm
Chamber radius	R	6	mm
Throat radius	$r_{ m throat}$	3.8	mm
Exit radius	$r_{ m exit}$	6.69	mm
Oxidizer injector length	$l_{\mathrm{O}_2}$	96	mm
Fuel injector length	$l_{\mathrm{CH_{4}}}$	44	mm
Length cylindrical chamber part	$l_{ m cyl}$	285	mm
Total chamber length	Ĺ	305	mm
Contraction ratio	$\varepsilon_{\rm con} = R^2/r_{\rm throat}^2$	2.5	_
Expansion ratio	$\varepsilon_{\rm con} = R^2/r_{\rm throat}^2$ $\varepsilon_{\rm exp} = r_{\rm exit}^2/r_{\rm throat}^2$	3.1	-

Table 1: Main dimensions of the TUM single-element combustor geometry

The thermocouples and uniformly distributed static pressure transducers provide quantitative measurement data from hot firing tests on axial wall temperature and pressure profiles in the cylindrical part of the chamber. Additionally, from the inverse heat transfer method according to Perakis et al. 16, the wall heat flux is reconstructed, which together with the pressure evolution serves to validate the modeling framework proposed in this work. The operating point and injection conditions analyzed in the following are summarized in Table 2.

For further details on the experimental setup and test campaign, refer to Silvestri et al.<sup>25,26</sup>.

Parameter	Symbol	Value	Unit
Chamber pressure	p	20	bar
Oxidizer mass flow rate	$\dot{m}_{ m O_2}$	0.03482	$kg s^{-1}$
Fuel mass flow rate	$\dot{m}_{ ext{CH}_4}$	0.01339	$kg s^{-1}$
Oxidizer temperature	$T_{\mathrm{O}_2}$	275	K
Fuel temperature	$T_{ m CH_4}$	269	K
Oxidizer-to-fuel ratio	O/F	2.6	_
Velocity ratio	$u_{\rm O_2}/u_{\rm CH_4}$	0.92	-
Density ratio	$ ho_{ m O_2}/ ho_{ m CH_4}$	1.95	-
Momentum ratio	$J = \rho_{\rm O_2} u_{\rm O_2}^2 / (\rho_{\rm CH_4} u_{\rm CH_4}^2)$	1.64	_

Table 2: Operating conditions of the TUM single-element combustor

# 3. Physical and Numerical Methodology

## 3.1 Flamelet-based combustion modeling framework

# 3.1.1 Classical flamelet approach

The flamelet concept is a widely used approach for efficient modeling of non-premixed combustion scenarios as typically present in rocket engine combustors. In the underlying model concept, the real-world highly complex turbulent flame structure evolving downstream of the propellants injection plane is abstracted by an ensemble of simple locally laminar counterflow diffusion flames, so-called flamelets, as illustrated schematically in Fig. 2. The depicted mixture fraction Z represents the first fundamental dimension of the flamelet manifold. This conservative scalar can be interpreted as the local fuel content in the mixture. In this study, it is determined using Bilger's definition based on element conservation<sup>21</sup>. The mixture fraction at stoichiometric mixing conditions is often used to identify the flame contour.

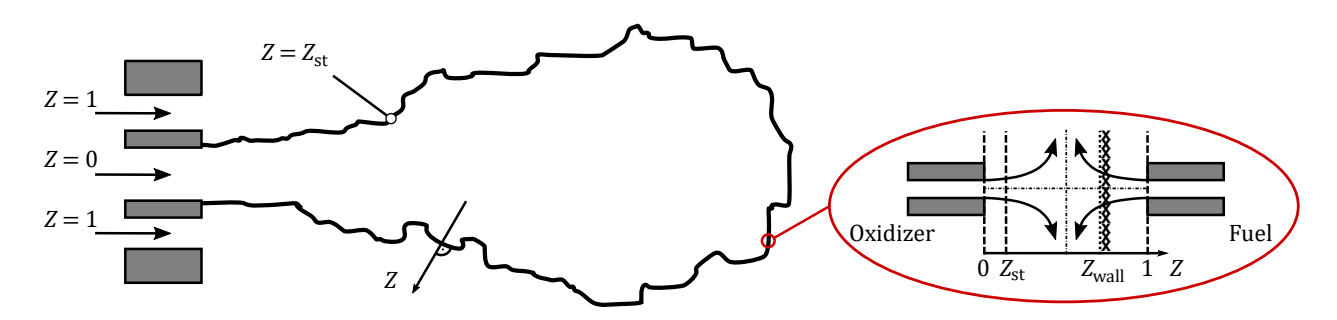


Figure 2: Schematic of the non-adiabatic flamelet concept

Expressed in physical space coordinates, this quasi-1D isobaric problem corresponds to the reacting axisymmetric stagnation point flow situation. Its governing system of equations comprises the conservation of mass, radial momentum, energy and mass fractions of participating chemical species and can be transformed directly into the mixture fraction space. In this coordinate system, used in the present study, all gradients whose line of action is not perpendicular to the iso-surface of the mixture fraction can be neglected<sup>20</sup>. The resulting so-called steady-state ( $\partial/\partial t=0$ ) flamelet equations, omitting differential mass diffusion, i.e. assuming a constant unity-Lewis number for each species  $\alpha$  ( $Le_{\alpha}=1$ ), become<sup>19</sup>:

$$0 = \frac{\chi}{2} \frac{\partial^2 Y_\alpha}{\partial Z^2} + \frac{\dot{\omega}_\alpha}{\rho} \tag{1}$$

$$0 = \frac{\chi}{2} \frac{1}{c_p} \left( \frac{\partial c_p}{\partial Z} + \sum_{\alpha} c_{p,\alpha} \frac{\partial Y_{\alpha}}{\partial Z} \right) \frac{\partial T}{\partial Z} + \frac{\chi}{2} \frac{\partial^2 T}{\partial Z^2} - \frac{1}{\rho c_p} \sum_{\alpha} h_{\alpha} \dot{\omega}_{\alpha}$$
 (2)

The introduced scalar dissipation rate  $\chi$  appearing as a coefficient in the convective and diffusive terms in the species transport and temperature equations results directly from the coordinate transformation and represents the counterpart to the physical strain rate, which describes the flow-induced flame stretching and wrinkling, thus incorporating finite rate effects. It characterizes the deviation from the chemical equilibrium, which is reached in the limiting case of theoretically infinitely fast chemistry at vanishing strain. The scalar dissipation rate acts as an inverse time scale and implicitly takes into account the influence of convection and diffusion perpendicular to the flame surface. Usually, an approach proportional to its stoichiometric value indicating the flame position and depending on the mixture fraction of the following form is chosen for its modeling:

$$\chi = \chi_{\rm st} \frac{f(Z)}{f(Z_{\rm st})} \tag{3}$$

To cover the full range of potentially occurring flame stretching states at a given background pressure, the flamelet equations have to be solved for a variety of scalar dissipation rate levels from approximated chemical equilibrium conditions at low values to the last burning configuration before flame extinction at high values. However, as a consequence of using the stoichiometric value of the scalar dissipation rate at the flame as the second look-up variable of the flamelet table, only these fully burned states on the stable upper branch of the so-called S-shaped curve can be incorporated unambiguously. Thus no dynamic flame effects such as partially extinguished states or transient re-ignitions are taken into account.

By means of the total differential of the mass-specific absolute enthalpy  $h = f(Y_a, T, p)$ 

$$dh = \sum_{\alpha} \frac{\partial h}{\partial Y_{\alpha}} \Big|_{Y_{\alpha} \neq Y_{\beta}, T} dY_{\alpha} + \frac{\partial h}{\partial T} \Big|_{Y_{\alpha}, p} dT + \frac{\partial h}{\partial p} \Big|_{Y_{\alpha}, T} dp = \sum_{\alpha} h_{\alpha} dY_{\alpha} + c_{p} dT + \frac{\partial h}{\partial p} \Big|_{Y_{\alpha}, T} dp$$

$$(4)$$

and considering the prevailing isobaric conditions ( $\partial p/\partial Z = 0$ ), a consistent flamelet energy conservation equation can also be established based on enthalpy:

$$0 = \frac{\partial^2 h}{\partial Z^2} \tag{5}$$

The enthalpy is therefore a linear function of the mixture fraction and represents a passive scalar whose shape depends exclusively on its boundary values. As the composition and the injection temperatures of the propellants are known and the background pressure is prescribed, its distribution in the entire solution field can be derived instantaneously

without having to solve a single equation. It consequently only acts as an equality constraint to the flamelet problem which is more favorable from a numerical point of view.

In order to close the flamelet equations, both a thermophysical modeling framework that is able to describe the relationship of pressure, temperature and specific volume, to link the thermal variables of state with the energetic ones and allows to infer the transport properties, as well as a reaction mechanism characterizing the chemical kinetics are required.

The moderate pressure levels and with respect to the individual critical points relatively high injection temperatures of the propellants examined in this study allow neglecting the intrinsic volume of the molecules and intermolecular forces such as attraction and mutual repulsion and therefore justify an ideal gas treatment. In this context of thermodynamic modeling, the density is determined from the ideal gas law:

$$\rho = \frac{pM}{RT} \tag{6}$$

The enthalpy and the specific isobaric heat capacity of the individual species are calculated from the most recent version of the NASA polynomials with nine coefficients  $^{4,15}$ . The caloric mixture quantities then result from the mass fraction-weighted average. For the determination of the dynamic species viscosities, the dilute gas approach according to the Chapman-Enskog kinetic theory  $^{22}$  is adopted. Based on these viscosities, the thermal conductivities of the species can then be deduced as proposed by Stiel and Thodos  $^{28}$ . The mixture transport properties are obtained analogously via mole fraction-weighted averaging.

To compute the chemical source terms, the skeletal reaction mechanism according to Sankaran et al.<sup>24</sup> is used, which is based on the detailed GRI-3.0 mechanism<sup>7</sup> for natural gas combustion and was optimized for fuel-rich combustion. The presence of nitrogen is neglected, which reduces the chemical mechanism further to 16 species and 71 elementary reactions.

Finally, to account for Turbulence-Chemistry Interaction (TCI), an integration of the laminar flamelet manifold is carried out using a presumed Probability Density Function (PDF)<sup>20</sup>. As described in Kim et al.<sup>9</sup>, the density-weighted Favre-averaged quantities  $\widetilde{\phi}$  such as specific heat capacity at constant pressure are calculated from:

$$\widetilde{\phi} = \int_0^\infty \int_0^1 \phi(Z, \chi_{st}) P(Z, \chi_{st}) dZ d\chi_{st}$$
(7)

while density-unweighted Reynolds averaged quantities  $\overline{\phi}$  such as the transport properties are determined via the following integral:

$$\overline{\phi} = \overline{\rho} \int_0^\infty \int_0^1 \frac{\phi(Z, \chi_{st})}{\rho(Z, \chi_{st})} P(Z, \chi_{st}) \, dZ \, d\chi_{st}$$
 (8)

where

$$\overline{\rho} = \left[ \int_0^\infty \int_0^1 \frac{1}{\rho(Z, \chi_{\text{st}})} P(Z, \chi_{\text{st}}) \, dZ \, d\chi_{\text{st}} \right]^{-1} \tag{9}$$

Statistical independence of the distributions of mixture fraction and stoichiometric scalar dissipation rate is usually postulated, which decouples the joint PDF to  $P(Z,\chi_{\rm st}) = P(Z)\,P(\chi_{\rm st})$ . While a  $\beta$ -PDF shape is adopted for the mixture fraction, which is parameterized by a given variance  $Z''^2$  around its mean value  $\widetilde{Z}$ , a simple log-normal or Dirac delta function is employed for the stoichiometric scalar dissipation rate. For a set of normalized mixture fraction variances

$$\widetilde{Z''^2}_{\text{norm}} = \frac{\widetilde{Z''^2}}{\widetilde{Z}(1-\widetilde{Z})}$$
 (10)

the turbulent flamelet manifold eventually yields:

$$\widetilde{\phi} = f\left(\widetilde{Z}, \widetilde{\chi}_{\text{st}}, \widetilde{Z''^2}_{\text{norm}}\right) \tag{11}$$

This pre-calculated multi-dimensional thermochemical database is used in the actual CFD simulation to interpolate quantities of interest at runtime solely based on the given governing access parameters. Instead of solving a transport equation for the mass fraction of almost each chemical species in each iteration step, only the scalar coupling parameters have to be determined. For detailed reaction mechanisms with an extensive number of species involved, this translates into a significant reduction in computational effort. However, the prerequisite for the validity of the classical flamelet

concept is that the zone in which chemical reactions and heat exchange take place is asymptotically thin compared to the turbulent length dimension, and that the chemical time scales are substantially smaller than the time scales representative for the fluid mechanical processes<sup>19</sup>. This manifests itself in a sufficiently high Damköhler number:

$$Da = \frac{\tau_{\text{flow}}}{\tau_{\text{chem}}} \begin{cases} \gg 1 & \to \text{ reactive} \\ \lesssim 1 & \to \text{ frozen} \end{cases}$$
 (12)

Consequently, although the turbulent eddies interact with the flame and cause its deformation and distortion, the diffusion of the propellants towards the reactive zone dominates the chemical species conversion.

## 3.1.2 Non-isobaric and non-adiabatic model extension

The classical flamelet concept, as introduced above, is limited to isobaric and adiabatic conditions. On the one hand, however, in order to adequately simulate an entire thrust chamber, an additional pressure dependency of the flamelet table is required. This extension is straightforward, as the process described above for solving the flamelet equations at varying degrees of stretching can be carried out at different background pressure levels. It should be emphasized that the resistance of the flame to stretching usually increases with pressure, which is why the highest stoichiometric scalar dissipation rate before quenching is pressure-dependent. For this reason, the flamelet manifold must be mapped to a global pressure-independent distribution. On the other hand, in addition, the gas expansion in the throat as well as in the nozzle extension further downstream is also directly coupled with a deviation from the adiabatic conditions. Moreover, the generally strongly cooled wall structures of the thrust chamber also extract a considerable amount of energy from the flow. One consequence are amplified exothermic chemical recombination effects, which increase the heat release, promote its transfer and ultimately also have an impact on the wall pressure profile, combustion efficiency and global performance characteristics. In order to adequately capture this heat loss, an enthalpy coordinate or some other kind of measure for the deviation from the adiabatic case must be added to the manifold. Many approaches for the non-adiabatic model extension have been proposed. Some of these proposals introduce additional source terms in the form of sinks into the flamelet equations, while others impose pre-assumed propellant-dependent shaped enthalpy distributions on the problem<sup>17,23</sup>. The most straightforward approach is to gradually reduce the enthalpy while maintaining the mixture composition of the adiabatic solution. However, disregarding the influence of heat extraction on the species mixture composition in the chemically frozen mixture fraction space can be an insufficient simplification when predicting wall heat loads. In the approach according to Wu and Ihme<sup>30</sup>, also successfully applied by Ma et al.<sup>14</sup>, Zips et al.<sup>31</sup> and Breda et al.<sup>3</sup>, on the other hand, a permeable, isothermal and chemically inert wall is introduced into the mixture fraction space as already indicated in Fig. 2. In this way, the flame is exposed to a heat loss that depends on the wall position  $Z_{\text{wall}}$  in a physical and universal manner. Each wall mixture fraction uniquely corresponds to a certain enthalpy level. The basic assumption made is that the heat flux is aligned with the mixture fraction gradient and that its line of action proceeds orthogonal to the flame front. The only mandatory requirement is that the prescribed wall temperature is chosen to be lower than the chemical activation temperatures involved. In the present study, it is set to be equal to the temperature at the fuel inlet. In order to mimic the coaxial injection situation in rocket combustion chambers with the fuel passing through the outer annular gap, in which particularly high enthalpy deficiencies are achieved at the combustion chamber wall at a rather fuel-rich mixture, the wall is placed at  $Z_{st} < Z_{wall} \le 1$ . In principle, however, the model also works in the oxidizer-rich mixture fraction regime. In this context, the adiabatic flamelet is just a special case, which is attained at  $Z_{\text{wall}} = 1$ . The permeable wall then has no impact on the solution field. In the procedure to cover the entire relevant enthalpy space, from this point, the wall is continuously advanced further into the domain towards the flame until a last burning configuration is reached at a certain pressure and stoichiometric scalar dissipation rate dependent minimum mixture fraction  $Z_{wall,lb}$ . A further reduction of  $Z_{wall}$ , similar to an excessive increase in strain, would again result in thermal quenching and flame extinction. The changing wall position implicitly entails a new time scale related to the convective heat transfer. However, since the assumption of a high Damköhler number is anchored in the underlying flame abstraction concept, the species composition is able to react quasi-instantaneously to the convective wall-induced cool-down of the mixture. This preserves solvability under steady-state conditions. Mathematically speaking, the presence of the permeable wall merely constitutes an additional internal thermal boundary condition. The cold wall itself represents an interface between the reacting, flame-containing region between the oxidizer inlet and the wall, where the classical flamelet equations are solved, and the inert diffusion-dominated mixing region between the wall and the fuel inlet, where the chemical source terms are deactivated:

 $0 < Z < Z_{\text{wall}}$ :

$$0 = \frac{\chi}{2} \frac{\partial^2 Y_\alpha}{\partial Z^2} + \frac{\dot{\omega}_\alpha}{\rho}, \quad 0 = \frac{\partial^2 h}{\partial Z^2}$$
 (13)

 $Z_{\text{wall}} < Z < 1$ :

$$0 = \frac{\partial^2 Y_\alpha}{\partial Z^2}, \quad 0 = \frac{\partial^2 h}{\partial Z^2} \tag{14}$$

In the non-reacting area behind the wall, the species mass fractions therefore also exhibit a linear progression, analogous to the enthalpy. At the wall itself, the profiles are continuously differentiable and therefore smooth. The absolute enthalpy at the wall, on the other hand, must be updated in each iteration step according to the current local mixture composition, the prescribed wall temperature and the constant operating pressure. The linear profiles on both sides of the wall result in:

$$h = \begin{cases} \frac{h_{\text{wall}} - h_{\text{ox}}}{Z_{\text{wall}}} Z + h_{\text{ox}} & \text{for } 0 \le Z \le Z_{\text{wall}} \\ \frac{h_{\text{fu}} - h_{\text{wall}}}{1 - Z_{\text{wall}}} (Z - Z_{\text{wall}}) + h_{\text{wall}} & \text{for } Z_{\text{wall}} < Z \le 1 \end{cases}$$
(15)

In summary, the boundary conditions that constitute the injection states and the coupling conditions to be defined at the permeable wall for the non-adiabatic flamelet problem read as follows:

Z=0:

$$h = h_{\text{ox}}, \quad Y_{\alpha} = Y_{\alpha, \text{ox}} \tag{16}$$

 $Z = Z_{\text{wall}}$ :

$$h = h_{\text{wall}}, \quad Y_{\alpha}|_{Z_{\text{wall}}^{-}} = Y_{\alpha}|_{Z_{\text{wall}}^{+}}, \quad \frac{\partial Y_{\alpha}}{\partial Z}|_{Z_{\text{man}}^{-}} = \frac{\partial Y_{\alpha}}{\partial Z}|_{Z_{\text{man}}^{+}}$$
(17)

Z = 1:

$$h = h_{\rm fu}, \quad Y_{\alpha} = Y_{\alpha, \rm fu} \tag{18}$$

The functional relationship between scalar dissipation rate and mixture fraction in Eq. (3), whose typical parameterization is inferred from a steady constant-density strained diffusion layer, is scaled to the reactive flame-containing range via the wall mixture fraction by Ma et al.<sup>13</sup>:

$$f(Z) = \exp\left[-2\left(\operatorname{erfc}^{-1}\left[2\frac{Z}{Z_{\text{wall}}}\right]\right)^{2}\right]$$
 (19)

However, since even this extension method for considering non-adiabatic states neither covers the entire enthalpy space achievable in the CFD simulation below the adiabatic enthalpy level nor includes a potential heat input, a combination of three different approaches is implemented in this work. First, several flamelets are calculated at different inlet temperatures without permeable wall influence, i.e.  $Z_{wall} = 1$ . For this purpose, the inlet temperatures of the propellants are increased and decreased with respect to the nominal values of the case under consideration. In the following, the percentage of the nominal injection temperatures is specified via the parameter  $\zeta_{T_{ini}}$ . This can already cover the enthalpy space to a certain extent, especially parts above the adiabatic level, and enables subsequent adjustments of the injection temperatures in the actual simulation with the exact same flamelet table, which significantly enhances its flexibility. The flamelet state with the lowest propellant temperatures at  $\zeta_{T_{\rm inj}, \rm min}$  is now starting point for varying the permeable wall position. As described, the wall is driven into the mixture fraction field up until the flame is extinguished due to excessive heat removal at  $Z_{\text{wall,lb}}$ . However, in order to capture the remaining enthalpy space between the last burning flamelet and the extinguished solution, the prevailing state is cooled at constant composition. The assumption in this case is a rapid quenching of the mixture preventing further chemical reactions. The degree of the frozen cool-down is quantified by the parameter  $\theta_{cool}$ . As an enthalpy reduction can only take place via the temperature under constant pressure and species mixture composition (cf. Eq. (4)), the temperature is reduced gradually and continuously, while the enthalpy is iteratively deduced. The temperature field results from:

$$T(Z) = \theta_{\text{cool}} T_{\text{inert}}(Z) + (1 - \theta_{\text{cool}}) T_{\text{lb}}(Z)$$
(20)

Consequently, at  $\theta_{\text{cool,max}} = 100 \%$ , the present mixture is abruptly cooled down to the temperature field that would hypothetically prevail for an inert mixing of the propellants consistent with the flamelet equations. In this way, for instance, even stoichiometric mixtures in low enthalpy environments, such as the near-wall region in strongly cooled

thrust chambers, would be available in the flamelet table.

To demonstrate this procedure, the enthalpy space encompassed for the methane combustion test case considered in this study is explored in the following at nominal combustion chamber pressure and a low stoichiometric scalar dissipation rate of  $\chi_{st} = 10^{-2} \text{ s}^{-1}$ , at which the departure of the in general quite stretch-resistant flamelet from the theoretically exact chemical equilibrium state is rather small.

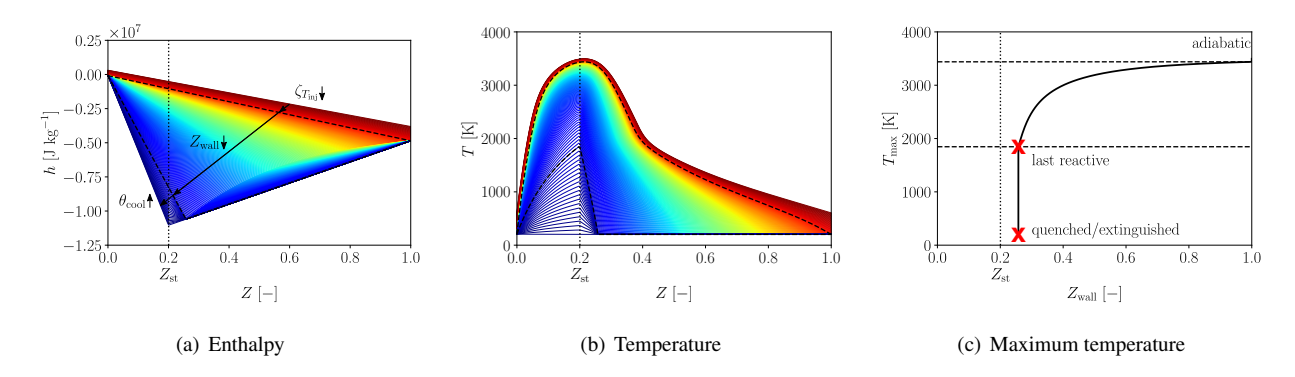


Figure 3: Mass-specific absolute enthalpy and temperature vs. mixture fraction and evolution of maximum flame temperature as a function of wall mixture fraction (i.e. covered part of adapted S-shaped curve)

In analogy to the classical S-shaped curve, which relates the maximum flame temperature with the inverse stoichiometric scalar dissipation rate, a similar curve can also be formed based on the wall mixture fraction. As far as the temperature is concerned, qualitatively, increasing the dissipation rate and thus the removal of energy and reaction products from the hot flame zone has the same effect as reducing the wall mixture fraction. While in the classical S-shape curve, the highest maximum flamelet temperature is reached asymptotically for the approximated chemical equilibrium  $\chi_{st} \approx 0 \text{ s}^{-1}$ , in this case, this upper limit corresponds to the value attained at highest propellant temperatures and Z<sub>wall</sub> = 1. Figure 3 shows this adapted S-shaped curve along with the flamelet solutions in terms of enthalpy and temperature. The stoichiometric mixture fraction  $Z_{st} \approx 0.2$  is indicated by a dotted line while the two interface flamelets between the three combined non-adiabatic model extension methods are highlighted by dashed lines. Starting from the adiabatic flamelet at lowest inlet temperatures  $\zeta_{T_{\rm inj}, \rm min} = 75$  %, the respective position of the permeable wall for  $Z_{\text{wall}} < 1$  can be identified by the kink between the two-sided linear enthalpy profiles. Due to the rising energy extraction from the flame zone and its convective transport via the cold isothermal wall as  $Z_{\text{wall}}$  decreases, a steepening of the temperature gradient with respect to the mixture fraction on the fuel-rich side of the flame and a decline in maximum temperature in the immediate vicinity of the stoichiometric mixing conditions can be observed, which is emphasized by the color coding of the isolines. Since the wall temperature is chosen to be identical to the lowest fuel temperature, the temperature between the wall and the fuel inlet is constant. At  $Z_{\text{wall,lb}} \approx 0.26$ , the last burning solution is encountered before the onset of thermal extinction under the given boundary conditions. However, as can be inferred from the visualized flamelet manifold fan, a large part of the enthalpy space is already covered before the frozen cool-down is performed.

As already mentioned, the influence of the enthalpy on the species composition is taken into account when solely changing the propellant inlet temperatures or applying the permeable wall method. Figure 4 depicts this development of the shape of the mass fraction profiles based on some of the major combustion products and chemical intermediate species as well as the volumetric heat release rate, which allows further flame characteristics to be deduced and is defined as:

$$\dot{\omega}_T = -\sum_{\alpha} \Delta h_{f,\alpha}^0 \dot{\omega}_{\alpha} \tag{21}$$

As expected, the local ratio of released CO to CO<sub>2</sub> is significantly reduced in low enthalpy environments. Likewise, the H<sub>2</sub>O content in the mixture grows globally. These observations are due to the low-temperature chemistry and the exothermic recombination effects. Chemical dissociation is suppressed as there is not sufficient energy available to break the molecular bonds. Reactions with lower required activation energy are promoted. The production rates and presence of radicals and intermediates such as OH or H<sub>2</sub> decrease monotonically with rising heat loss across the cold wall in favor of the stable main combustion products, which in turn increase the net energy release due to their lower standard enthalpies of formation. With the same enthalpy loss, this leads to a lower temperature decrement than would result from the simplifying assumption of a frozen mixture composition. The heat release as well as the energy

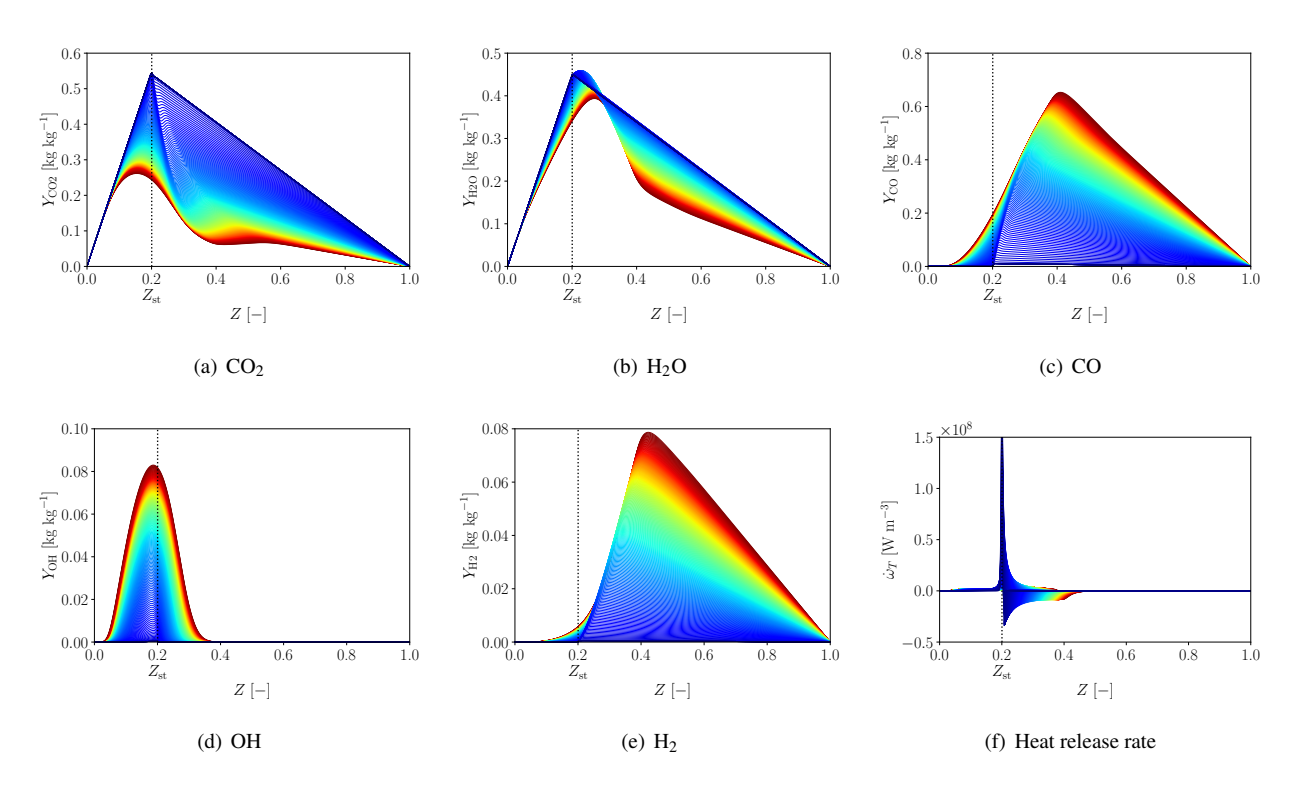


Figure 4: Mass fractions of selected chemical species and volumetric heat release rate vs. mixture fraction

consumption, which characterizes the decomposition of the fuel, is condensed at low enthalpy levels to a thin region near the stoichiometric mixture fraction. Integrally, the volumetric heat release rate diminishes, while the flame front becomes progressively more confined.

At this point, it should be noted that the enthalpy distribution in the mixture fraction space is a result of the flamelet equations that depends on the prevailing pressure and the stoichiometric scalar dissipation rate. However, in order to avoid an inverse table look-up for the enthalpy level during the CFD simulation, a mapping onto a global enthalpy distribution is performed in the same manner as for the stoichiometric dissipation rate. Furthermore, for the sake of simplicity and to avoid further expanding the dimensionality of the flamelet manifold, a delta function PDF is also assumed for pressure and enthalpy in the integration procedure, which ultimately leads to an extended thermochemical library of the form

$$\widetilde{\phi} = f\left(\widetilde{Z}, \widetilde{\chi}_{\text{st}}, \widetilde{Z''^{2}}_{\text{norm}}, \overline{p}, \widetilde{h}\right)$$
(22)

which is discretized by 96 million data points in total for the simulation test case of this study.

The Portable, Extensible Toolkit for Scientific Computation (PETSc)<sup>1,2</sup>, which can be supplied with the residual functions of the mathematical problem at hand from Python via the interface PETSc4Py<sup>6</sup>, is employed for the iterative solution of the system of partial differential equations describing the flamelet state. It allows to tackle the steady-state problem either directly or to integrate it with additional robustness enhancing transient terms via a pseudo time-stepping technique and the linearly implicit Euler method from the time-stepping (TS) module. The Newton line search algorithm with cubic backtracing from the Scalable Nonlinear Equation Solvers (SNES) library is employed for the outer non-linear problem. The Generalized Minimum Residual (GMRES) Krylov subspace method is used to invert the inner linear equation system, where an incomplete LU decomposition (ILU) is performed for preconditioning, which counteracts the stiffness introduced by the chemical source terms. The Jacobian matrix is efficiently approximated by second order finite differences. The chemical equilibrium state serves as initial solution, which is determined using the fast element potential method under adiabatic and isobaric conditions<sup>27</sup>.

## 3.2 Governing equations

In the CFD simulation, the time-averaged compressible Navier-Stokes equations, comprising the continuity equation and the conservation equation for momentum and energy formulated on the basis of enthalpy, are solved. The laminar heat flux vector included in the energy equation is calculated via Eq. (4) based on the transported enthalpy, enabling its divergence to be treated implicitly. Due to the ideal gas treatment, the contributions due to pressure changes can be neglected. Dissipation caused by viscous stresses, on the other hand, is taken into account in form of the viscous heating source term, since the nozzle flow characterized by high Mach numbers is considered in the following. The averaged pressure-velocity term is approximated. In addition, the discussed flamelet model requires the solution of the transport equations for the mixture fraction and its variance, as well as an algebraic model expression for the scalar dissipation rate, which, according to its definition, reflects the proportional relationship between the mixture fraction variance and an integral turbulent time scale. In summary, the following coupled set of averaged governing equations is obtained:

$$\frac{\partial \overline{\rho}}{\partial t} + \frac{\partial (\overline{\rho} \widetilde{u}_i)}{\partial x_i} = 0 \tag{23}$$

$$\frac{\partial \overline{\rho}}{\partial t} + \frac{\partial (\overline{\rho u_i})}{\partial x_i} = -\frac{\partial \overline{p}}{\partial x_i} + \frac{\partial}{\partial x_i} \left[ (\overline{\mu} + \mu_t) \left( \frac{\partial \overline{u_i}}{\partial x_j} + \frac{\partial \overline{u_j}}{\partial x_i} - \frac{2}{3} \frac{\partial \overline{u_k}}{\partial x_k} \delta_{ij} \right) - \frac{2}{3} \overline{\rho} k \delta_{ij} \right]$$
(24)

$$\frac{\partial \left(\overline{\rho}h\right)}{\partial t} + \frac{\partial \left(\overline{\rho}\widetilde{u_i}h\right)}{\partial x_i} = \frac{\partial \overline{p}}{\partial t} + \widetilde{u_i}\frac{\partial \overline{p}}{\partial x_i} + \frac{\partial}{\partial x_i} \left[ \left(\frac{\overline{\lambda}}{c_p} + \frac{\mu_t}{Pr_t}\right)\frac{\partial \widetilde{h}}{\partial x_i} \right] + \overline{\mu} \left(\frac{\partial \widetilde{u_i}}{\partial x_j} + \frac{\partial \widetilde{u_j}}{\partial x_i} - \frac{2}{3}\frac{\partial \widetilde{u_k}}{\partial x_k}\delta_{ij}\right)\frac{\partial \widetilde{u_i}}{\partial x_j}$$
(25)

$$\frac{\partial \left( \overline{\rho} \widetilde{Z} \right)}{\partial t} + \frac{\partial \left( \overline{\rho} \widetilde{u}_i \widetilde{Z} \right)}{\partial x_i} = \frac{\partial}{\partial x_i} \left[ \left( \frac{\overline{\lambda}}{\overline{c}_p} + \frac{\mu_t}{Sc_t} \right) \frac{\partial \widetilde{Z}}{\partial x_i} \right]$$
(26)

$$\frac{\partial \left( \overline{\rho Z''^2} \right)}{\partial t} + \frac{\partial \left( \overline{\rho u_i} \widetilde{Z''^2} \right)}{\partial x_i} = \frac{\partial}{\partial x_i} \left[ \left( \frac{\overline{\lambda}}{\widetilde{c_p}} + \frac{\mu_t}{Sc_t} \right) \frac{\partial \widetilde{Z''^2}}{\partial x_i} \right] + 2 \frac{\mu_t}{Sc_t} \left( \frac{\partial \widetilde{Z}}{\partial x_i} \right)^2 - \overline{\rho \chi_{st}}$$
(27)

$$\widetilde{\chi}_{\rm st} = 2\frac{\epsilon}{k} \widetilde{Z''^2} \tag{28}$$

The closure of the unclosed terms emerging from the Favre averaging of the instantaneous and exact balance equations is based on the Boussinesq assumption. Phenomenological similarity between molecular diffusion and turbulent fluctuations is postulated in such a way that the momentum exchange of interacting particles or vortices equally leads to viscous or turbulent stresses and is determined by the mean shear rate. In accordance with the laminar Stokes hypothesis for Newtonian fluids, a turbulent eddy viscosity is thus introduced. In a so-called gradient-diffusion approach, the turbulent fluxes are then correlated to this scalar quantity and the mean local gradient similarly to their respective laminar counterparts. Under the assumption of isotropy, the description of turbulence is thus reduced to the determination of the eddy viscosity. This is achieved in the present study using the standard k- $\epsilon$  turbulence model according to Launder and Spalding 12, which requires the solution of the following two further transport equations for the turbulent kinetic energy and its dissipation rate:

$$\frac{\partial \left(\overline{\rho}k\right)}{\partial t} + \frac{\partial \left(\overline{\rho}u_{i}k\right)}{\partial x_{i}} = \frac{\partial}{\partial x_{i}} \left[ \left(\overline{\mu} + \frac{\mu_{t}}{\sigma_{k}}\right) \frac{\partial k}{\partial x_{j}} \right] + \left[ \mu_{t} \left( \frac{\partial \overline{u}_{i}}{\partial x_{j}} + \frac{\partial \overline{u}_{j}}{\partial x_{i}} - \frac{2}{3} \frac{\partial \overline{u}_{k}}{\partial x_{k}} \delta_{ij} \right) - \frac{2}{3} \overline{\rho}k \delta_{ij} \right] \frac{\partial \overline{u}_{i}}{\partial x_{j}} - \overline{\rho}\epsilon$$
(29)

$$\frac{\partial \left(\overline{\rho}\epsilon\right)}{\partial t} + \frac{\partial \left(\overline{\rho}\widetilde{u}_{i}\epsilon\right)}{\partial x_{i}} = \frac{\partial}{\partial x_{i}} \left[ \left(\overline{\mu} + \frac{\mu_{t}}{\sigma_{\epsilon}}\right) \frac{\partial \epsilon}{\partial x_{j}} \right] + C_{\epsilon,1} \frac{\epsilon}{k} \left[ \mu_{t} \left( \frac{\partial \widetilde{u}_{i}}{\partial x_{j}} + \frac{\partial \widetilde{u}_{j}}{\partial x_{i}} - \frac{2}{3} \frac{\partial \widetilde{u}_{k}}{\partial x_{k}} \delta_{ij} \right) - \frac{2}{3} \overline{\rho} k \delta_{ij} \right] \frac{\partial \widetilde{u}_{i}}{\partial x_{j}} - C_{\epsilon,2} \overline{\rho} \frac{\epsilon^{2}}{k}$$
(30)

The turbulent viscosity is then determined from:

$$\mu_{\rm t} = C_{\mu} \bar{\rho} \frac{k^2}{\epsilon} \tag{31}$$

All model constants in the transport equations for the turbulence quantities are set to standard values. For improved wall treatment, the two-layer approach as proposed by Wolfshtein<sup>29</sup> is used. A constant value of  $Pr_t = 1.2$  is specified for the turbulent Prandtl number, while  $Sc_t = 0.7$  is assumed for the turbulent Schmidt number. It has been found that this combination of settings provides the best numerical predictions.

The pressure-based coupled solution algorithm of the commercial code ANSYS Fluent was utilized for the steady-state simulation. Second-order-accurate central differencing schemes were used for the spatial discretization. The reading and processing routines of the presented 5D flamelet model were realized via the user-defined function solver interface.

## 3.3 Computational setup

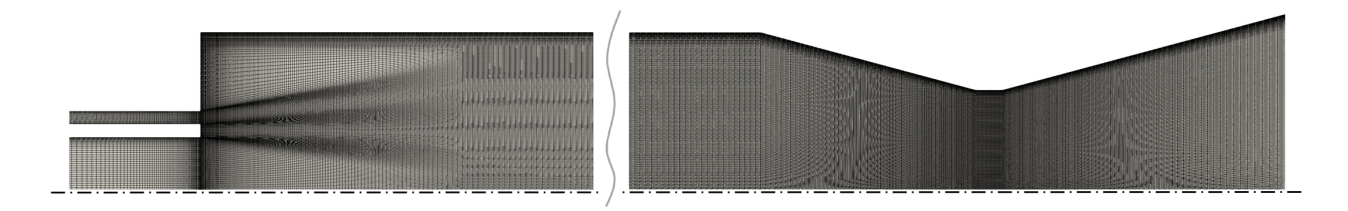


Figure 5: Computational grid

Since the entire spectrum of turbulent scales is modeled via a statistical approach in this study and only the mean flow field is actually solved, the symmetry properties of the combustor geometry under consideration can be exploited, thus saving considerable computational effort. The 2D axisymmetric mesh used in this study contains approximately 300,000 cells and is shown in Fig. 5. The injector lip is discretized with 50 cells. Furthermore, to resolve the boundary layer properly down to the viscous sublayer, the grid is refined near the wall such that the condition  $y^+ < 1$  is fulfilled at all wall boundaries. For this purpose, an initial wall-normal distance to the first cell center of 5  $\mu$ m in the chamber as well as 1  $\mu$ m in the injectors and nozzle is required, while 50  $\mu$ m at faceplate and post is sufficient. The full injector lengths are taken into account in order to achieve more realistic turbulent flow profiles in the injection plane.

The experimentally measured mass flow rates and static temperatures are applied to the inlets as boundary conditions. At the outlet, the static ambient pressure is specified. No-slip conditions are imposed on all walls. The faceplate and the oxidizer post are modeled as adiabatic, while the interpolated reconstructed temperature profile is prescribed at the walls of the cylindrical part of the chamber. As there is no reliable measurement data available for the hot gas side wall temperature in the nozzle, the temperature of the last data point is used consistently.

# 4. Results

To visualize the developing steady flow field and the established mixture conditions, contour plots of the velocity magnitude with superimposed streamlines and the mixture fraction are depicted in Fig. 6. For illustrative purposes, the complete representation of the flow conditions upstream of the injection plane is omitted and the simulation domain characterized by a high aspect ratio is axially compressed. The streamlines reveal a relatively strongly radially deflected fuel jet. In addition, a typical pronounced fuel-rich recirculation area at the faceplate is striking. Further downstream, the streamlines are increasingly aligned parallel to the wall and considerably more uniform. The injector arrangement with the fuel entering through the outer annular gap leads to a fuel-rich mixture composition on the entire chamber wall surface. In contrast, as expected, oxidizer-rich conditions are found at the axis while an area-weighted average mixture fraction of  $Z \approx 0.28$  is eventually present at the nozzle exit.

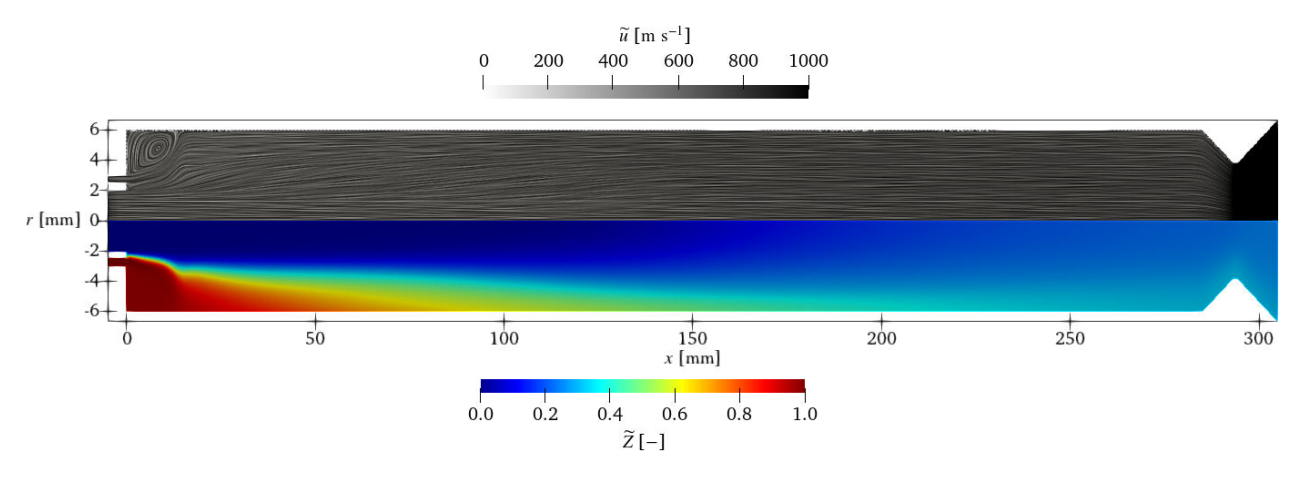


Figure 6: Contour plots of velocity magnitude with superimposed streamlines (top) and mixture fraction (bottom) with clipped injectors and axially compressed domain

In analogous manner, the resulting temperature field and a logarithmically scaled contour of the volumetric heat release rate are given in Fig. 7. It is immediately apparent how the incoming oxidizer pushes the flame anchored to the post outwards. The combustion heat is mainly generated in the evolving reacting shear layer. In this region, the spatial gradients of the state variables are particularly high. The conversion of the chemical energy bound in the propellant molecules into thermal and potential energy causes the temperature to rise steeply. It then flattens out progressively in the core flow until the flow field homogenizes. Only in the pronounced thermal boundary layer at the chamber walls and during the conversion process of static pressure and thermal energy into kinetic energy within the divergent part of the nozzle clear temperature variations are still visible. The flame length can be estimated based on the depicted isoline of the stoichiometric mixture fraction. It extends up to  $x \approx 250$  mm. Despite the low shear forces due to the arising velocity ratio of the injected propellants (cf. Table 2), an effective mixture can be established such that the flame contour is closed within the combustion chamber. At  $x \approx 100$  mm, the flame expands radially and forms a convex bulge following the recirculation area at the faceplate. Downstream of the intersection point of the isoline of stoichiometric mixture conditions and the chamber axis, the energy release decays steadily. This finally marks the end of the active combustion zone.

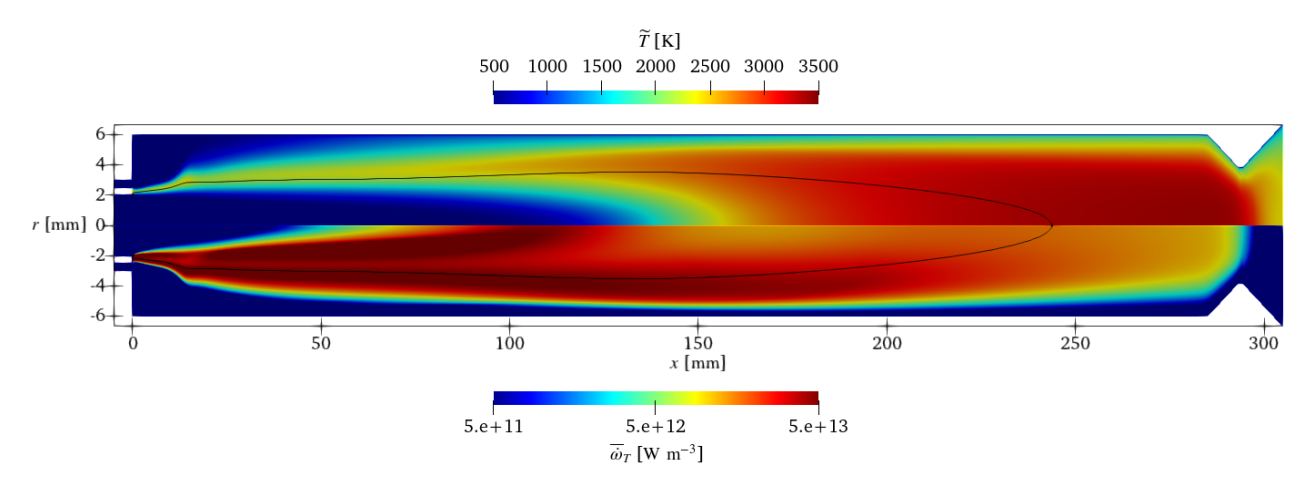


Figure 7: Contour plots of temperature (top) and volumetric heat release rate (bottom) (logarithmically scaled) with clipped injectors and axially compressed domain. Isoline of stoichiometric mixture fraction indicated.

The mass fraction fields of  $CO_2$  and CO are represented in Fig. 8. Due to the lack of oxidizer in the fuel-rich recirculation area and near the chamber walls, CO has a large share in the composition whereas in the bulk flow and especially in the nozzle  $CO_2$  is dominant. Only in the immediate vicinity of the wall it is the other way around. The heat losses due to the cold wall promote chemical recombination effects and the ratios have shifted in favor of the  $CO_2$  concentration.

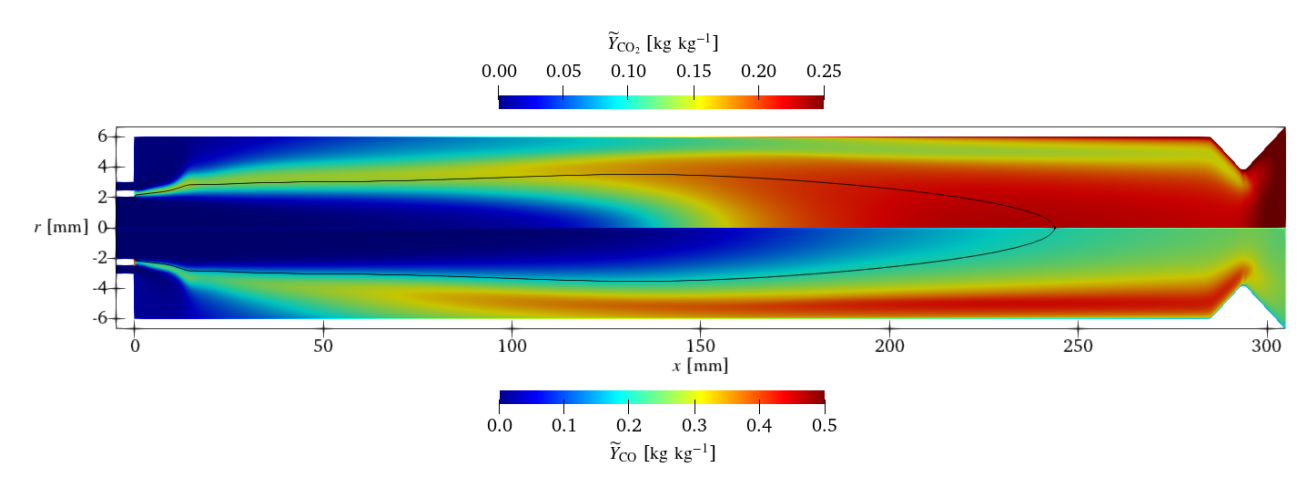


Figure 8: Contour plots of CO<sub>2</sub> (top) and CO (bottom) mass fraction with clipped injectors and axially compressed domain. Isoline of stoichiometric mixture fraction indicated.

For a more in-depth analysis of the species conversion process, Fig. 9 contains the radial profiles of the temperature

and selected species mass fractions at three axial locations, which can be assigned to different combustion regimes. The radial coordinate is normalized to the combustion chamber radius. At x = 50 mm, the already mentioned sharp temperature peak with a monotonic drop can be observed both in the direction towards the wall and towards the symmetry axis. This also applies analogously to the mass fractions shown, each of which has a maximum with a steady decline on both sides. Further downstream of the zone near the injector at x = 150 mm, a turning point in the distribution of  $CO_2$  and  $CO_2$  and  $CO_3$  and  $CO_4$  and  $CO_3$  and  $CO_4$  a

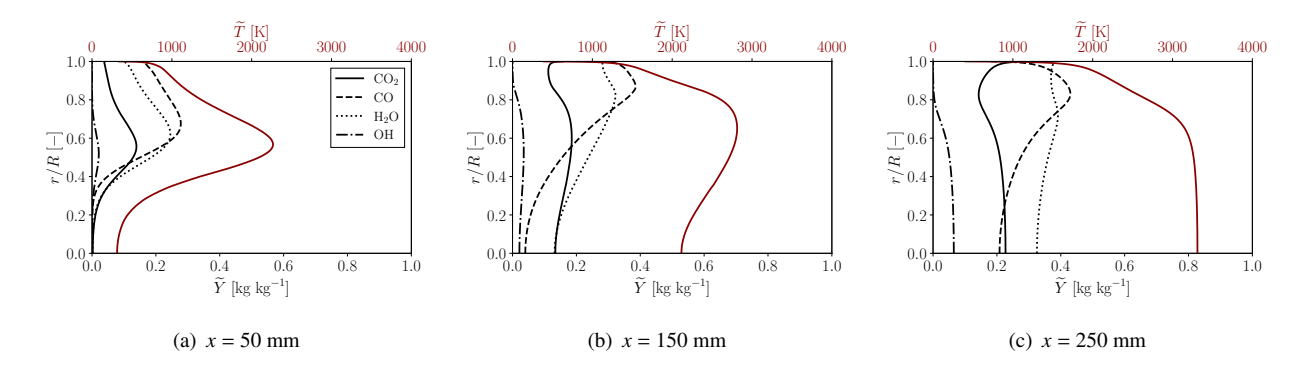


Figure 9: Radial profiles of selected species mass fractions and temperature at different axial locations

The scatter plots of enthalpy and temperature over the mixture fraction in Fig. 10 reveal that a large space of states is spanned across the chamber. For orientation, the highest and lowest enthalpy levels at nominal combustion chamber pressure and the evaluated stoichiometric scalar dissipation rate from the analysis in Fig. 3 are incorporated. In the fuel-rich post-reaction zone containing the nozzle, regions of particularly low enthalpy levels are reached, which can be derived from the coloration of the state space based on pressure. In the steady-state solution shown, these states are primarily covered by the permeable wall method. However, enthalpy levels in the frozen cool-down domain were also attained in intermediate steps of the solution process. In addition, state points with near stoichiometric mixing conditions and enthalpies above the adiabatic level at nominal propellant injection temperatures can be identified. These states correspond in principle to excess heat and reinforce the necessity of varying the injection temperatures beyond the nominal values when generating the flamelet table. It can be concluded that the presented flamelet model covers all states occurring throughout the solution process without exception only by combining the presented methods for the non-adiabatic extension of the classical modeling approach.

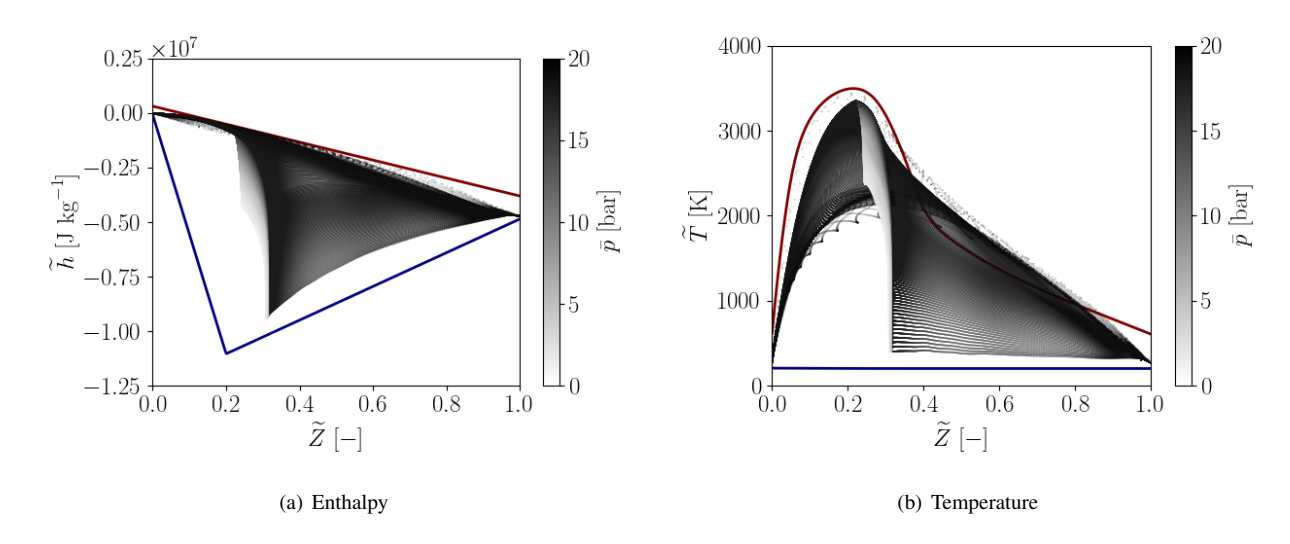


Figure 10: Scatter plots of mass-specific absolute enthalpy and temperature vs. mixture fraction (colored by pressure)

Finally, Fig. 11 presents the comparison with the measured wall pressure profile and the reconstructed wall heat flux along the chamber axis. The magnitude of both quantities can be reproduced correctly. Without exception, the pressure arising in the numerical simulation remains within the estimated error bars which have to be taken into account due to measurement uncertainties. Moreover, there is also a largely good qualitative agreement with the experimental data. The initial slight increase in pressure due to the recirculating vortex structure in the corner between the faceplate and combustion chamber wall as well as the subsequent extended drop associated with the flame-induced acceleration of the burnt gas are well predicted by the simulation. Only the flattening of this pressure drop, which indicates a decay of the exothermic chemical conversion, is not accurately captured. The apparent overestimation of the flame length in the simulation can also be concluded from the shape of the wall heat flux. While the monotonic increase is reproduced properly, the inversely determined data set shows a maximum at  $x \approx 200$  mm with subsequent slightly decreasing values. In the simulation, however, the wall heat flux remains approximately constant at this maximum level in the shown cylindrical chamber part. In addition, the heat load near the injector is underestimated. The retrospectively ascertained heat flux shows a much more significant plateau before it continues to rise steadily.

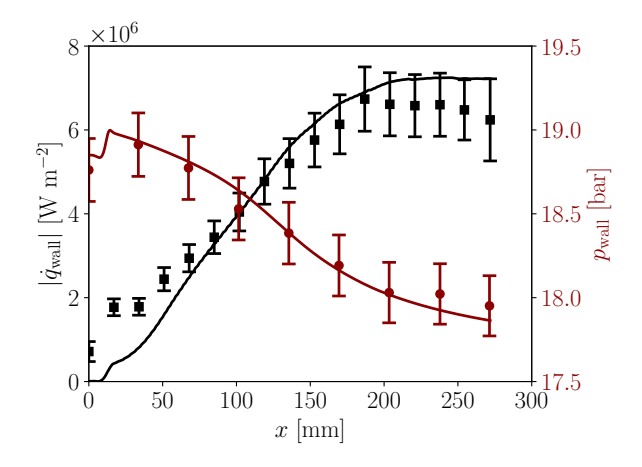


Figure 11: Comparison of simulation results with experimental measurements in terms of wall heat flux and pressure profile along the chamber axis

# 5. Conclusions

In the present work, an efficient flamelet-based combustion and heat transfer modeling framework was implemented, which can be applied to reacting rocket thrust chamber flows featuring high pressure and enthalpy variations. By combining the variation of the injection temperatures, the introduction of the permeable, isothermal and chemically inert wall into the mixture fraction space and a subsequent frozen cool-down, heat input and a substantial heat loss associated with strongly cooled chamber walls as well as its influence on the chemical species conversion and energy release can be captured by the multi-dimensional flamelet table. The propellant combination considered in this context is arbitrary, as all the methods used are self-contained and do not necessitate any additional case-dependent parameter calibration.

To demonstrate the effectiveness and performance of this model, it was applied to a methane combustion configuration under conditions representative for rocket engine operation. Both macroscopic flame characteristics and the behavior of the thermal boundary layer as well as the change in the species mixture composition driven by recombination reactions, especially at the cold chamber wall, were investigated in detail. Overall, satisfactory results were achieved in comparison with available experimental measurement data in terms of wall pressure and heat flux. It remains to be analyzed to what extent the disregard of 3D effects affects the numerical predictions with respects to the complex vortex system near the injectors as well as the total flame length. Furthermore, it should be verified whether the choice of a relatively high turbulent Prandtl number required to meet the wall heat load level can be attributed to the limitation of the basic model assumptions to the regime of high Dahmköhler numbers. At least in the immediate vicinity of the wall and within the nozzle, the ratio of the characteristic time scales is expected to change significantly. Premature freezing of the mixture could suppress further exothermic chemical recombination effects and thus reduce the wall heat flux. Moreover, a comparison with numerical results obtained with more sophisticated approaches of turbulence modeling and high-fidelity finite rate chemistry could be performed.

## References

- [1] S. Balay, S. Abhyankar, M. F. Adams, S. Benson, J. Brown, P. Brune, K. Buschelman, E. Constantinescu, L. Dalcin, A. Dener, V. Eijkhout, J. Faibussowitsch, W. D. Gropp, V. Hapla, T. Isaac, P. Jolivet, D. Karpeev, D. Kaushik, M. G. Knepley, F. Kong, S. Kruger, D. A. May, L. C. McInnes, R. T. Mills, L. Mitchell, T. Munson, J. E. Roman, K. Rupp, P. Sanan, J. Sarich, B. F. Smith, S. Zampini, H. Zhang, and J. Zhang. *PETSc/TAO Users Manual*, ANL-21/39 Revision 3.2, Argonne National Laboratory. 2024.
- [2] S. Balay., W. D. Gropp, L. C. McInnes, and B. F. Smith. Efficient Management of Parallelism in Object Oriented Numerical Software Libraries. *Modern Software Tools in Scientific Computing*, pages 163–202, 1997.
- [3] P. Breda, M. Pfitzner, N. Perakis, and O. J. Haidn. Generation of non-adiabatic flamelet manifolds: comparison of two approaches applied on a single-element GCH4/GO2 combustion chamber. In *EUCASS*, 2019.
- [4] A. Burcat and B. Ruscic. Third Millennium Ideal Gas and Condensed Phase Thermochemical Database for Combustion with Updates from Active Thermochemical Tables. ANL-05/20 TAE 960, Argonne National Laboratory, 2005.
- [5] H. Burkhardt, M. Sippel, A. Herbertz, and J. Klevanski. Kerosene vs. Methane: A Propellant Tradeoff for Reusable Liquid Booster Stages. *Journal of Spacecraft and Rockets*, 41(5):762–769, 2004.
- [6] L. D. Dalcin, R. R. Paz, P. A. Kler, and A. Cosimo. Parallel Distributed Computing Using Python. *Advances in Water Resources*, 34(9):1124–1139, 2011.
- [7] GRI-MECH3.0. http://combustion.berkeley.edu/gri-mech, visited 10.03.2024.
- [8] A. Iannetti, N. Girard, D. Tchou-kien, C. Bonhomme, N. Ravier, and E. Edeline. Prometheus, a LOX/LCH4 Reusable Rocket Engine. *Proceedings of the 7th European Conference for Aeronautics and Space Sciences*, 2017.
- [9] S.-K. Kim, M. Joh, H. S. Choi, and T. S. Park. Multidisciplinary Simulation of a Regeneratively Cooled Thrust Chamber of Liquid Rocket Engine: Turbulent Combustion and Nozzle Flow. *International Journal of Heat and Mass Transfer*, 70:1066–1077, 2014.
- [10] I. A. Klepikov, B. I. Katorgin, and V. K. Chvanov. The New Generation of Rocket Engines, Operating by Ecologically Safe Propellant 'Liquid Oxygen and Liquified Natural Gas (Methane)'. *Acta Astronautica*, 41(4-10):209–217, 1997.
- [11] O. Knab, H. Riedmann, B. Ivancic, C. Höglauer, M. Frey, and T. Aichner. Consequences of Modeling Demands on Numerical Rocket Thrust Chamber Flow Simulation Tools. In *Progress in Propulsion Physics Volume 11*, pages 317–346. EDP Sciences, 2019.
- [12] B.E. Launder and Spalding. Lectures in Mathematical Models of Turbulence. Academic Press (London), 1972.
- [13] P. C. Ma, H. Wu, M. Ihme, and J.-P. Hickey. A Flamelet Model with Heat-Loss Effects for Predicting Wall-Heat Transfer in Rocket Engines. In *53rd AIAA/SAE/ASEE Joint Propulsion Conference*. American Institute of Aeronautics and Astronautics, 2017.
- [14] P. C. Ma, H. Wu, M. Ihme, and J.-P. Hickey. Nonadiabatic Flamelet Formulation for Predicting Wall Heat Transfer in Rocket Engines. *AIAA Journal*, 56(6):2336–2349, 2018.
- [15] B. J. McBride, M. J. Zehe, and S. Gordon. NASA Glenn Coefficients for Calculating Thermodynamic Properties of Individual Species. *Tech. rep. NASA*, 2002.
- [16] N. Perakis and O. J. Haidn. Inverse heat transfer method applied to capacitively cooled rocket thrust chambers. *International Journal of Heat and Mass Transfer*, 131:150–166, 2019.
- [17] N. Perakis, C. Roth, and O. J. Haidn. Development of a Non-Adiabatic Flamelet Model for Reacting Flows with Heat Loss. In *Proceedings of the Space Propulsion*. 2018.
- [18] N. Peters. Laminar Diffusion Flamelet Models in Non-Premixed Turbulent Combustion. *Prog. Energy Combust. Sci.*, 10(3):319–339, 1984.

- [19] N. Peters. Laminar Flamelet Concepts in Turbulent Combustion. *Symposium (International) on Combustion*, 21:1231–1250, 1986.
- [20] N. Peters. Turbulent Combustion. Cambridge University Press, 2010.
- [21] H. Pitsch and N. Peters. A Consistent Flamelet Formulation for Non-Premixed Combustion Considering Differential Diffusion Effects. *Combustion and Flame*, 114:26–40, 1998.
- [22] B. E. Poling, J. M. Prausnitz, and J. P. O'Connell. *The Properties of Gases and Liquids*. McGraw-Hill Education, New York, 5th edition, 2001.
- [23] D. Rahn, H. Riedmann, R. Behr, and O. J. Haidn. Non-Adiabatic Flamelet Modeling for the Numerical Simulation of Methane Combustion in Rocket Thrust Chambers. In *Joint Propulsion Conference*. American Institute of Aeronautics and Astronautics, 2018.
- [24] R. Sankaran, E. R. Hawkes, J. H. Chen, T. Lu, and C. K. Law. Structure of a spatially developing turbulent lean methane air Bunsen flame. *Proceedings of the Combustion Institute*, 31(1):1291–1298, 2007.
- [25] S. Silvestri, M. P. Celano, C. Kirchberger, G. Schlieben, O. J. Haidn, and O. Knab. Investigation on Recess Variation of a Shear Coax Injector for a Single Element GOX-GCH4 Combustion Chamber. *Transactions of the Japan Society for Aeronautical and Space Sciences, Aerospace Technology Japan*, 14:13–20, 12 2016.
- [26] S. Silvestri, M.P. Celano, O.J. Haidn, and O. Knab. Comparison of Single Element Rocket Combustion Chambers with Round an Square Cross Sections. In *EUCASS*, 2015.
- [27] W. R. Smith and R. W. Missen. Chemical Reaction Equilibrium Analysis: Theory and Algorithms. 1983.
- [28] L. I. Stiel and G. Thodos. The thermal conductivity of nonpolar substances in the dense gaseous and liquid regions. *AIChE Journal*, 10:26–30, 1964.
- [29] M. Wolfshtein. The velocity and temperature distribution in one-dimensional flow with turbulence augmentation and pressure gradient. *International Journal of Heat and Mass Transfer*, 12(3):301–318, 1969.
- [30] H. Wu and M. Ihme. Modeling of Wall Heat Transfer and Flame/Wall Interaction A Flamelet Model with Heat-Loss Effects. *Proceedings of the 9th U. S. National*, 2015.
- [31] J. Zips, C. Traxinger, P. Breda, and M. Pfitzner. Assessment of Presumed/Transported Probability Density Function Methods for Rocket Combustion Simulations. *Journal of Propulsion and Power*, 35(4):747–764, 2019.